PAPER

Check for updates

Entropy engineering in I–V–VI$_2$ family: a paradigm to bestow enhanced average *ZT* in the entire operating temperature regime†

Ranita Basu, [ID] *[ab] U. Sandhya Shenoy, [ID] [c] Ankita Pathak,[ab] Shweta Singh,[bd] P. Jha, [ID] [ab] D. Krishna Bhat, [ID] [e] Hirakendu Basu [ID] [bd] and Ajay Singh[ab]

The design and development of n-type alloys in the mid-temperature regime (500–700) K with enhanced thermoelectric performance is of utmost necessity for the fabrication of thermoelectric devices. In this regard, the I–V–VI$_2$ family reveals superior thermoelectric performance, owing to the fact that group V elements have non-bonded electrons and high Z (atomic number), with a high Grüneisen parameter, which cause amplified anharmonicity and subsequently low intrinsic lattice thermal conductivity. However, the irony is that the well-studied alloy of this family, AgBiSe$_2$, undergoes phase transition in the operating temperature range. Thus, of paramount importance is restricting the phase transition and bringing it down below room temperature (RT), along with stabilizing a highly symmetrical crystal structure in the extended operating temperature range. Efforts were made to synthesize a cubic n-type AgBiSeS alloy belonging to the I–V–VI$_2$ compounds (unlike AgBiSe$_2$) that is stabilized throughout the temperature range, as the S element aids in strengthening of the chemical bonds. In addition, the alloy was further stabilized by forming a solid solution with PbSe, which aids in increasing the configurational entropy and thereby increases the chemical space of the system. The resultant alloys possess intrinsically low lattice thermal conductivity ranging from 0.38–0.74 W m^{-1} K^{-1} in the entire operating range. Consequently, the peak ZT was reported as ∼0.6 at 780 K, with an average ZT value of 0.3 for the alloy (AgBiSeS)$_{0.5}$(PbSe)$_{0.5}$ within 300–823 K. Although the reported ZT is low, the methodology of entropy-driven structural stabilization in the operating temperature regime was adapted to attain a highly symmetrical, stable structure for practical applications.

1. Introduction

In today's environment of looming global energy scarcity, the pursuit of unconventional power generation methods is of extreme importance. One of the promising alternatives is thermoelectric power generation. Its ability to recover waste heat (which accounts for about two-thirds of the consumed fossil fuel) and convert it to electrical energy makes it suitable

for manifold industrial applications. Moreover, thermoelectric (TE) modules involve no moving parts, which makes them portable and highly reliable and increases their operational life.[1–6] Their reliability has been shown in space applications, where they have operated without failure for more than 30 years.[7,8] The particular demand from energy system developers and industrial component manufacturers for high-temperature thermo-generators has significantly accelerated institutional and governmental research efforts worldwide. However, today's available devices cannot be applied at temperatures higher than 250 °C, yet the largest part of recoverable waste heat is available at those temperatures. Thus, an urgent need in research progress is required to explore technically viable solutions at elevated temperatures. Nevertheless, low conversion efficiency and high cost limit their usage in niche applications. With substantial improvement in the figure-of-merit (ZT), which requires untangling two unfavorably coupled properties, thermoelectric materials can be used in more advanced applications, which include harvesting waste heat from power plants and engines or cooling computer chips. The

a Technical Physics Division, Bhabha Atomic Research Centre, Mumbai 400085, India. E-mail: ranitapaul@gmail.com, ranitab@barc.gov.in; Tel: (+91)2225593217

b Homi Bhabha National Institute, Training School Complex, Anushaktinagar, Mumbai 400094, India

c Department of Materials Science and Engineering, Institute of Engineering and Technology, Srinivas University, Mukka 574146, Mangalore, Karnataka, India

d Analytical Chemistry Division, Bhabha Atomic Research Centre, Mumbai 400085, India

e Department of Chemistry, National Institute of Technology Karnataka, Surathkal, Srinivasnagar 575025, Mangalore, Karnataka, India

† Electronic supplementary information (ESI) available. See DOI: https://doi.org/10.1039/d4ma00549j

dimensionless ZT of the material is given by: $ZT = (\alpha^2\sigma/(\kappa_e + \kappa_l))T$, where α, σ, κ_e, and κ_l are the Seebeck coefficient, electrical conductivity, electronic thermal conductivity and lattice thermal conductivity, respectively. Thus, (i) decoupling of α, σ, and κ_e through band engineering to improve the power factor[9,10] and (ii) phonon engineering through lattice defects[11] and embedding nanostructures which destroy the path required for the propagation of the phonons[12] are the two mainstream stratagems for boosting the thermoelectric performance. In the past decade, several new thermoelectric elements were designed and discovered, and notably, entropy engineering has evolved as an exemplar shifting methodology which integrates the phase, band and phonon engineering via multi-component alloying. Entropy engineering is actually a hybrid of the research fields in conventional thermoelectrics and high-entropy alloys (HEAs).[13–15] Here, the participation of the multiple elements tends to form high-symmetry crystal structures, *i.e.*, face-centered cubic lattice or body-centered cubic lattice, which are otherwise thermoelectrically preferred due to the introduction of high band degeneracy, Nv, and thus leads to a high Seebeck coefficient, α. This can also be explained from the fact that the influence of entropy of mixing, $-T\Delta S_{conf}$, counterbalances the strain energy and hence stabilizes the crystalline single-phase solid solution.[16] The influence of the enhanced entropy effect is so influential that in some instances, a single-phase alloy is formed, violating the classic Hume–Rothery rules. Thus, the hypotheses of "enhanced entropy" and configurational entropy-stabilized compounds are useful to elucidate the stability challenge. Nevertheless, the entropy-driven, structurally stabilized single phase provides a beneficial path to strengthen the electrical transport properties with some incremental compromise in the carrier mobility.[17]

According to a well-recognized report, high-performance thermoelectric materials, in principle, are degenerate semiconductors possessing high crystal symmetry and the lowest lattice thermal conductivity. Traditional thermoelectric materials with rock salt cubic structure (SG: $Fm\bar{3}m$), for instance, PbTe,[18–20] SnTe[21–24] and PbSe,[14,25,26] were intensely studied in the past owing to their superior thermoelectric performance. These alloys possess multiple valleys, having carrier pockets with a copious number of equivalent positions in a typical reciprocal space benefitting from high crystal symmetry. In order to explore new thermoelectric materials, researchers are now inclined towards extending their interest to the ternary I–V–VI$_2$ alloys with crystal structure similar to $AgSbTe_2$.[27–30] This alloy is considered as an isoelectronic structural analog of the champion thermoelectric alloy, PbTe. $AgSbTe_2$ crystallizes in rock-salt structure at room temperature and has appeared to be a promising thermoelectric material due to low lattice thermal conductivity, restricted by the Sb lone pair electrons. Moreover, Roychowdhury *et al.* have demonstrated that by optimizing the electronic and phonon transport properties simultaneously, Cd-doped $AgSbTe_2$ exhibits a near-room-temperature ZT of $\sim$1.5 and a max ZT of 2.6 at 573 K, which is one of the highest ever reported among the state-of-the-art bulk TE alloys from room temperature to 573 K.[29] Nevertheless, $AgSbTe_2$ shows p-type conduction intrinsically and is difficult to tune into n-type via the addition of dopants. Moreover, the n-type counterpart of $AgSbTe_2$ with a similar rock salt crystal structure is absent in the ternary I–V–VI$_2$ family. This largely restricts the realistic application of this particular family of materials for the fabrication of thermoelectric modules, which demands both n- and p-type legs manufactured from alloys with similar physical and chemical properties.[31]

To confront this challenge, $AgBiSe_2$ was discovered from the same I–V–VI$_2$ family as a matched n-type counterpart. However, $AgBiSe_2$ undergoes polymorphic transition twice in the operating temperature regime: (i) 390–525 K, from hexagonal (α) to rhombohedral (β), and (ii) from rhombohedral (β) to cubic (γ) in the temperature span of 560–585 K.[32–36] These phase transitions impose a serious threat because as far as thermoelectric modules are concerned, sudden changes in the crystal structure and lattice constants would engender high internal stress in the device.[37] This phase transition can be averted largely by considering the Ag–Bi–Se–S system, which is intrinsically n-type with NaCl crystal structure, and thus the thermoelectric community deviated their focus from the parent compound. AgBiSeS (or BiAgSeS) belongs to the extensively studied parent compound $AgBiSe_2$ alloy (I–V–VI$_2$ system) and has been described as an established n-type alternative with the unusually low thermal conductivity of 0.29 W m^{-1} K^{-1} at 823 K due to the presence of heavy-mass elements and frail inter-atomic bonding.[38] The cubic daughter alloy AgBiSeS is stabilized owing to the S residing at the Se site and imparts modifications in the bond length and bond angle, which eventually can cause distortion in the crystal structure and thus reduce the lattice thermal conductivity.[39] Hu *et al.* mentioned that AgBiSeS crystallizes in cubic phase at high temperature, and room-temperature cubic phase is vulnerable towards synthetic procedures. Utmost care was taken to synthesize AgBiSeS in order to retain the cubic structure.[40] Furthermore, it was manifested that enhancing the configurational entropy of AgBiSeS via entropy engineering can ascertain the cubic structure in the entire operating temperature range and averts the sudden spike in internal thermal stress.[41] In this regard, AgBiSeS was alloyed with PbSe because it aids in the enhancement of chemical space. PbSe was chosen for alloying, as it is a well-proven high-performance thermoelectric material, along with compensating the loss of Se in the synthetic procedure. AgBiSeS shows n-type conduction, and to maintain the conduction type on alloying and to avoid the energy barrier due to the formation of p–n junction, n-type PbSe was chosen. This paradigm utilizes multiple elements to occupy the indistinguishable atomic sites and eventually augment the stability of the highly symmetrical crystal structure.

2. Experimental

The synthetic procedure, characterization techniques and the computational details employed in this study are described in ESI† (S1.0).

3. Results and discussions

3.1. Influence of the alloying of PbSe on the structural and chemical properties of AgBiSeS

Fig. 1(a) shows the room-temperature powder XRD pattern of $(AgBiSeS)_{1-x}(PbSe)_x$ for the melt-alloyed and hot-pressed samples. The samples crystallize in cubic rock salt (NaCl) structure, and the major Bragg peaks match well with the simulated AgBiSeS structure. AgBiSeS, which belongs to the I–V–VI$_2$ compounds (unlike AgBiSe$_2$) due to its S element, has strengthened chemical bonds, and thus, the cubic structure is stabilized.[40] Moreover, the XRD pattern demonstrates that the cubic structure is retained even upon alloying with PbSe. The slight shifting of the peaks to lower 2θ degree with the increase in the PbSe content indicates competition for the cationic site by the large Pb^{2+} ion. In other words, the experimental observation can be attributed to the overall compensation by the replacement of the cationic site (Ag–Bi disordered occupation) by the larger ionic radius of Pb, and the anionic site by more Se atoms. As aforementioned, the vulnerability of the cubic phase of AgBiSeS at RT towards the methodology adapted for synthesis demands highly sensitive DSC measurement to be carried out in order to ascertain that no phase transition takes place in the operating temperature regime. The measurement manifested high thermal stability with no thermal sign (endothermic or exothermic peak) owing to entropy engineering (Fig. 1(b)). The thermal stability of the PbSe-alloyed AgBiSeS with the composition $(AgBiSeS)_{0.5}(PbSe)_{0.5}$ was further confirmed by high-temperature XRD plot (Fig. S1, ESI†). According to the laws of thermodynamics, entropy (S) is considered as a gauge to understand the microscopic configuration of the arrangement, and relying on the Boltzmann hypothesis, for a multispecies system, the entropy of mixing is given by: $\Delta S_{mix} = -R \sum_{i=1}^{n} x_i \ln C x_i$, where R is the universal gas constant and x_i is defined as the molar concentration of the ith constituent.[42] Although for pristine AgBiSeS, $\Delta S_{mix} = 0$, with the increasing concentration of PbSe, the configurational entropy increases and attains maximum for $x = 0.5$ and then decreases. Fig. 1(c) shows the plot of calculated ΔS_{mix} *vs.* x for the $(AgBiSeS)_{1-x}(PbSe)_x$ solid solution, and Fig. 1(d) demonstrates the schematic of temperature *vs.* composition plot, or more precisely, the phase diagram inferred from powder XRD and DSC analysis. The plot depicts that the novel engineered alloy is stabilized due to enhanced configurational entropy.

A topical analysis of the cubic stabilized pristine dimetal chalcogenide, AgBiSeS, exhibits a Raman active mode E$_g^2$ for Bi–Se bonding at ~121.6 cm^{-1} that demonstrates the presence of macroscopic polarizability in the molecule (Fig. 2(a)). Actually, in cubic AgBiSeS, having cubic structure at room temperature and enhanced configurational entropy in comparison to AgBiSe$_2$ (theoretical and structural analyses unveiled the presence of two Raman active modes in the hexagonal lattice of AgBiSe$_2$ at room temperature owing to the presence of two types of Bi atom at 124 cm^{-1} and 157 cm^{-1} assigned to E$_g$ and A$_{1g}$ modes), the cationic disorder due to Ag vacancy and Bi$_{Ag}$ antisite defect fetch only one Raman peak at room temperature.[43] However, metal ions or cations exist in altogether disordered state at ambient temperature on alloying due to the increase in configurational entropy and presence of antisite defects. This makes the
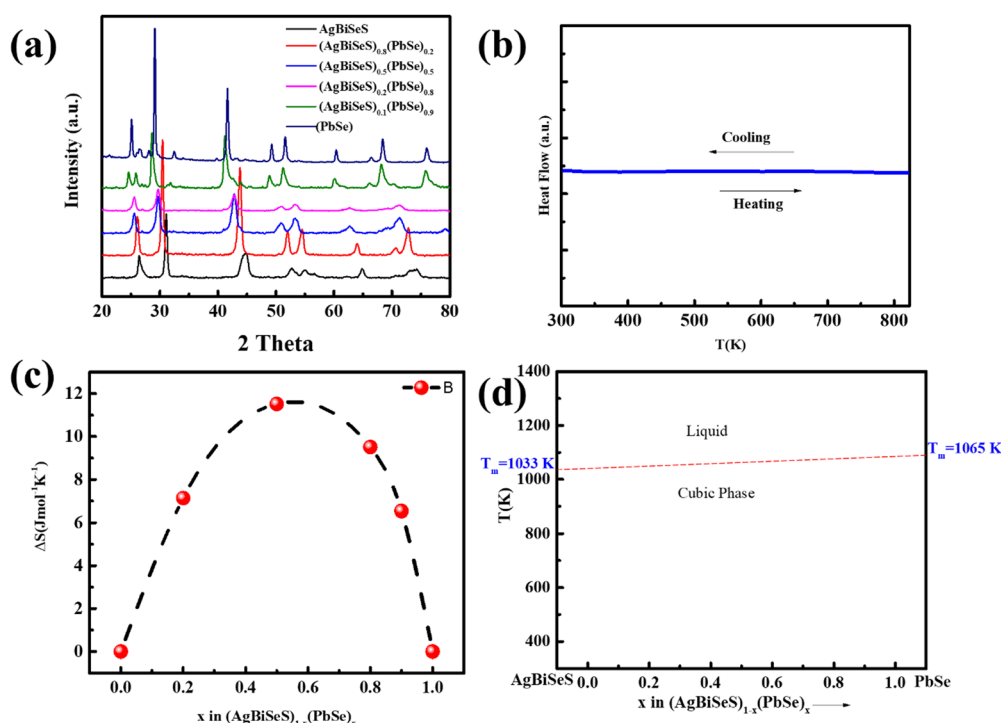

Fig. 1 (a) Room-temperature XRD pattern of $(AgBiSeS)_{1-x}(PbSe)_x$ (x = 0, 0.2, 0.5, 0.8, 0.9, 1.0); (b) DSC curve for the alloy system; (c) calculated configurational entropy *vs.* composition parameter x for $(AgBiSeS)_{1-x}(PbSe)_x$ (x = 0, 0.2, 0.5, 0.8, 0.9, 1.0); (d) schematic of temperature-composition plot for the pseudo-binary alloy system depicting stabilized cubic structure in the entire temperature regime.
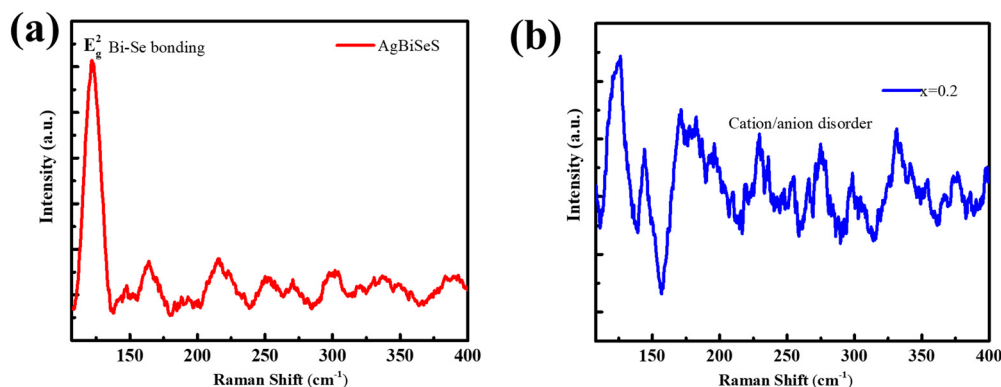
Fig. 2 (a) Room-temperature Raman spectra of AgBiSeS and $(AgBiSeS)_{0.8}(PbSe)_{0.2}$ illustrating how the increase in the configurational entropy aids in disorder in the system, which eventually evades the Raman peak.

exchange of metal ions inevitable, or in other words, the formation of vacancies (vacancy defects) acts like a passage in the exchange of the metal ions and thus plays a major role.[44] To rephrase, the cationic intermixing or disordering causes no macroscopic polarizability and evades the Raman peak, owing to the absence of long-range ordering of atoms (which is a basis of the Raman peak) (Fig. 2(b)).

The enclosed bonding nature of pristine AgBiSeS, as shown in Fig. 3(a), and of $(AgBiSeS)_{1-x}(PbSe)_x$ ($x = 0.2$) (Fig. S2, ESI†), was further corroborated by X-ray photoelectron spectroscopy (XPS). The elements Ag, Bi, Pb, Se and S were clearly spotted in the survey scan, and to identify the chemical state, high-resolution spectra were acquired for the aforementioned elements. In the Ag

3d XPS spectrum, the Ag $3d_{5/2}$ can be deconvoluted by the Ag curve fitting software into two peaks. The peaks centred at 367.1 eV ($3d_{5/2}$) and 373.1 eV ($3d_{3/2}$) are attributed to +1 oxidation state and assigned to the Ag–Se bond.[45] Similarly, the peaks at 367.94 eV ($3d_{5/2}$) and 373.94 eV ($3d_{3/2}$) correspond to Ag–S bond.[46] The high-resolution scan of Bi 4f (Fig. 3(b)) shows two strong, broad peaks with binding energies of 157.7 eV and 163.02 eV corresponding to Bi $4f_{7/2}$ and $4f_{5/2}$, respectively, which are assigned to the Bi–Se bond, with Bi primarily in the +3 oxidation state.[47] In addition, the peaks at 159.6 eV and 164.9 eV correspond to Bi 4f7/2 and 4f5/2, respectively, of the Bi–S bond.[48] The occurrence of spin orbit separation ($\sim$1.2 eV) between S $2p_{3/2}$ (161.1eV) and S $2p_{1/2}$ (162.3 eV) peaks corroborate the presence of
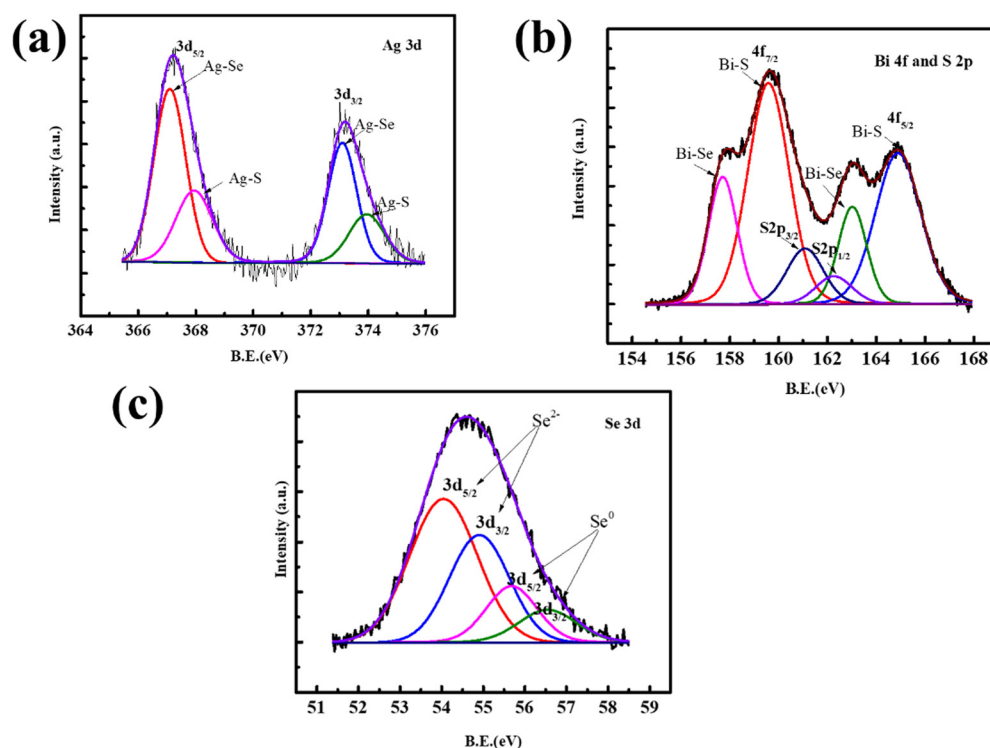

Fig. 3 (a) X-ray photoelectron spectra: (a) Ag-3d; (b) Bi-4f and S-2p; (c) Se-3d.

S in the form of S^{2-} in the alloy (Fig. 3(b)). The high-resolution scan for 3d Se corresponds to selenides as well as Se in elemental state (Fig. 3(c)). Analogous to sulphides, the existence of spin orbit separation of ($\sim$0.86 eV) between Se $3d_{5/2}$ (54.05 eV) and Se $3d_{3/2}$ (54.91 eV) confirms the presence of selenides in the alloy. However, commenting on the exact chemical environment of the Se is difficult because the binding energy values corresponding to Bi–Se and Ag–Se are close by and beyond the resolution of our instrument. Moreover, suppressing the loss of Se vapor is also enabled by the presence of elemental Se in the alloy. To corroborate the XPS analysis, analogous to AgBiSeS, Huang *et al.* reported the cubic structure of AgBiSeTe at room temperature and studied the local structure using X-ray absorption fine structure spectroscopy (XAFS). They explicitly mentioned that the local structure of Bi in AgBiSeTe is more disordered in comparison to AgBiSe$_2$ and AgBiTe$_2$, although the antisite disorder prevails in all the alloys. In addition, when the radial distribution function is compared for the Bi L$_3$-edge and Se K-edge for AgBiSe$_{1-x}$Te$_x$ (x = 0, 0.5, 1.5 and 2) using extended X-ray absorption fine structure spectroscopy (EXAFS), the analysis revealed that the Bi–Te bond crops up and intensifies with increasing Te content. However, when probed at the Se K-edge, all the peaks are well aligned for the first shell and correspond to Se–Bi or Se–Ag bonds.[49] Using similar analogy, it can be interpreted that when probed at the Bi L$_3$-edge in AgBiSeS, there will be pronounced Bi–S bond, whereas probing at the Se K-edge will show Se–Bi or Se–Ag bonds. Thus, the depiction of the schematic representation of the arrangement of atoms is shown in Fig. S3 (ESI†).

As aforementioned, unlike AgBiSe$_2$, S residing at the Se (Fig. S3, ESI†) site will modify the bond length and bond angle, and thus, the bond heterogeneity will eventually contribute to the reduction of lattice thermal conductivity.

3.2. Electronic transport behaviour and electronic structure calculation

The temperature-dependent Seebeck coefficient (Fig. 4(a)) was recorded from 300 to 823 K, and the negative value for both pristine AgBiSeS and PbSe indicates n-type conduction (Fig. S4(a), ESI†). Interestingly, the Seebeck coefficient for AgBiSeS was very high, $\sim$−620 μV K^{-1} at 300 K, and it decreases with temperature to $\sim$−150 μV K^{-1} at 825 K. Jang *et al.* explained that in the ABX$_2$ system, it is the B-site cation which dictates the conduction type. For Sb-based alloys, *i.e.*, B═Sb, the alloy imparts p-type conduction, whereas for Bi-based alloys, *i.e.*, B═Bi, the alloys show n-type conduction. Thus, the n-type conduction in AgBiSeS is presumably due to the Bi$_{Ag}$, *i.e.*, Bi- on Ag antisite defect, and the enhanced Seebeck coefficient is due to the high effective mass (m^*).[50] Moreover, the decrease in Seebeck coefficient with increase in temperature can be ascribed to the effect of bipolar conduction, *i.e.*, the presence of contrasting charge carriers or two different electron bands with varied effective mass (violation of single parabolic mode).[38] In other words, calculation of the effective mass in n-type AgBiSeS is complex owing to non-parabolicity of the conduction band in the proximity of Fermi level. Nevertheless, in the interest of simplicity and to acquire a rough estimation of the effective mass of the carriers, the single parabolic band model was considered.

Moreover, to validate the assumption, m^* was evaluated using the following equations utilizing experimental Seebeck coefficient, S and carrier density (n_H) measured at 300 K (eqn (1)–(3)):

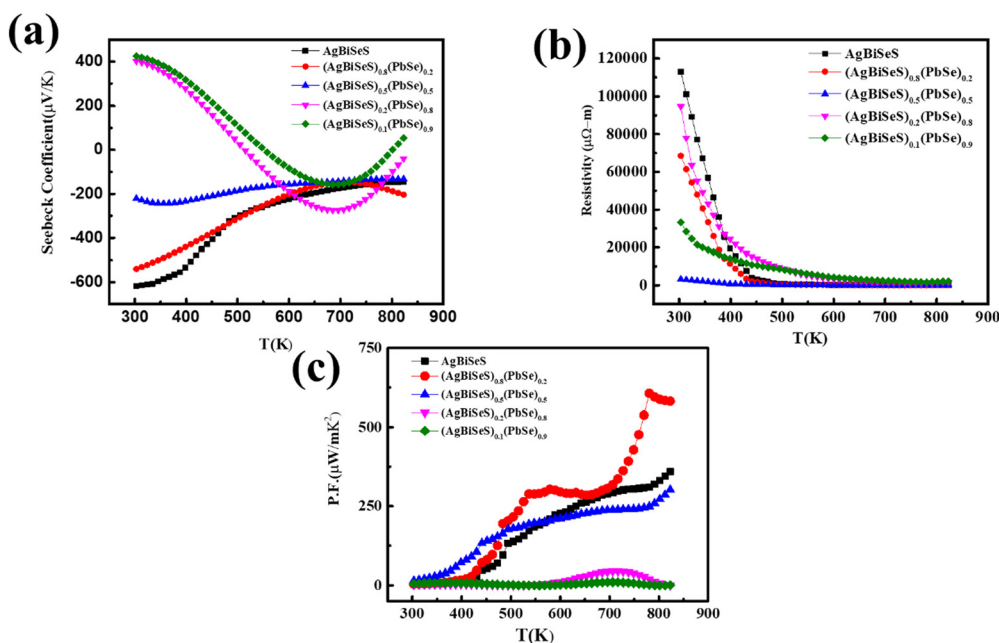$$m^* = \frac{h^2}{2k_\beta T}\left[\frac{n}{4\pi F_{1/2}(\eta)}\right]^{2/3} \tag{1}$$

Fig. 4 Temperature-dependent (a) Seebeck coefficient; (b) electrical resistivity and (c) power factor of the alloy system (AgBiSeS)$_{1-x}$(PbSe)$_x$.
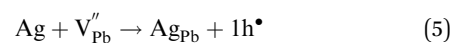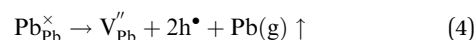
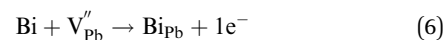$$S = \pm \frac{k_\beta}{e}\left(\frac{(r+3/2)F_{r+3/2}(\eta)}{(r+3/2)F_{r+1/2}(\eta)} - \eta\right) \quad (2)$$

$$F_n(\eta) = \int_0^\infty \frac{x^\eta}{1+e^{x-\eta}}dx \quad (3)$$

where r is the scattering factor, e is the electron charge, h is Planck's constant, and k_β, η and $F_n(\eta)$ denote the Boltzmann constant, reduced Fermi energy and nth order Fermi integral, respectively. The reduced Fermi energy was computed by fitting the resultant experimental Seebeck data. For simplicity, $r = -1/2$ was considered for acoustic phonon scattering, which is assumed to be the main scattering mechanism at ambient temperature and remains independent of the grain size. The reduced Fermi energy, η, was derived from the fitted Seebeck coefficient, and the effective mass (m^*) was calculated to be $0.36m_0$. The optimised effective mass in comparison to other state-of-art thermoelectric alloys corroborate the high Seebeck coefficient values. However, the m^* owing to the presence of high Z elements reduces carrier mobility drastically and is thus responsible for the high resistivity of the alloy. Thus, apart from the motivation of entropy engineering, a solid solution of AgBiSeS and PbSe was formed to optimise the quasi-independent parameters and aid in obtaining a sweet spot of high figure-of-merit in the ZT vs. T plot. Surprisingly, the point which needs to be discussed is that although both AgBiSeS and PbSe show n-type conduction, the trend of Seebeck coefficient vs. T is different owing to the difference in the band structure or carrier concentration. For pure AgBiSeS, as discussed earlier, the Seebeck coefficient is very high, and with increase in temperature, it diminishes owing to the fact that the thermal excitation of charge carriers moderates the Seebeck coefficient. However, PbSe, being a degenerate semiconductor, undergoes electron–electron scattering with the rise in temperature, and hence, the Seebeck coefficient is enhanced (for reference, the electronic and thermal transport properties of PbSe are shown in Fig. S4(a–f), ESI†). In the case of solid solution, $(AgBiSeS)_{1-x}(PbSe)_x$, for $x = 0.2$ and 0.5, the variation of α vs. T follows the trend of AgBiSeS, where the conduction type is determined by the Bi_{Ag} antisite defect, i.e., the holes created by the acceptor atom (Ag) are compensated by the electrons donated by the donor atom (Bi). Nevertheless, the trend is mysterious for $x = 0.8$ and 0.9, where the alloy undergoes p–n transition, i.e., shows p-type conduction in the temperature regime of (300–550) K, and beyond that, n-type conduction, where the Seebeck coefficient increases in the negative direction, attaining maximum at ~ 650 K and then showing an upturn. In principle, for a multinary compound with high-symmetry cubic crystal structure, cation disordering is profound, and it has implication on the electronic properties. As discussed earlier, the B site cation determines the conduction type, and the lone pair on the B-site cation bestows intense phonon–phonon scattering and predominantly diminishes the lattice thermal conductivity. Although the stereochemical activity of the lone pair on the cation is impeded by the formation of ABXY, which interrupts the polymorphic transition, high symmetry is exhibited by increasing the chemical space, which subsequently increases the configurational entropy

by surpassing the enthalpy change in the Gibb's free energy equation. Nevertheless, in $(AgBiSeS)_{0.2}(PbSe)_{0.8}$ and $(AgBiSeS)_{0.1}(PbSe)_{0.9}$, both Ag^{1+} and Bi^{3+}, being minor, occupy the Pb^{2+} site based on the size of the ionic radii. PbSe with octahedral geometry exhibits the ionic radius of Pb^{2+} as 133 pm, whereas Bi^{3+} and Ag^{1+} have the ionic radii of 103 pm and 115 pm, respectively. Thus, due to the close proximity of the cationic radii, both Bi^{3+} and Ag^{1+} can occupy the Pb^{+2} site. However, Jang et al. explicitly mentioned that antisite defects are provoked when the electronegativity difference between the atoms are inconsequential.[50] For instance, the thermochemical electronegativity values of Ag, Bi and Pb are 1.93, 2.02 and 1.87, respectively, in Pauling's scale. Thus, exchange of the atoms would not affect the bonding characteristics significantly. However, the formation energy values are important to understand the feasibility of the antisite defect. Shannon mentioned that in $AgBiSe_2$, the formation energy of Bi_{Ag} is lower in comparison to Ag_{Bi}, apparently due to the smaller ionic radii of Bi^{3+} than Ag^{1+} in an octahedral site.[51] This causes charge compensation by electrons donated by Bi^{3+} ion to the holes created by the Ag vacancies (V_{Ag}) having acceptor-like tendency. Since Ag vacancies accept only one electron, the $AgBiSe_2$ system has surplus electrons and thus shows n-type conduction. This shows that the charged antisite defect can cause n-type polarity and dispels the customary notion of n-type conduction via controlling the Se vacancy. Rather, the low formation energy of the donor-type antisite defect facilitates n-type conduction in the alloy. If a similar analogy prevails, then the Pb vacancy, V_{Pb}, in PbSe (loss at anionic site, Se^{2-} is supersaturated with Se vapour) induces p-type conduction;[52] thus, the Ag^{1+} cation occupies the V_{Pb} site, forming the antisite defect of Ag_{Pb}. This is highly probable and expected to have low formation energy owing to the fact that Ag^{1+} and Pb^{2+} have comparable ionic radii. Thus, the cation disordering due to the formation of the charged antisite defect Ag_{Pb} is highly probable and feasible. However, Ag can donate only one electron to the Pb-site, and an extra hole remains uncompensated, and thus, the composite with $x = 0.8$ and 0.9 shows p-type conduction at ambient temperature. Thus, it is obvious that in the present study, at ambient temperature, the conduction type (p-type) is determined by the following eqn (4) and (5):

$$Pb_{Pb}^\times \rightarrow V_{Pb}^{''} + 2h^\bullet + Pb(g) \uparrow \quad (4)$$

$$Ag + V_{Pb}^{''} \rightarrow Ag_{Pb} + 1h^\bullet \quad (5)$$

During the thermal disorder process, the Ag–Bi atom exchange results in a quasi-metallic state, bringing more conduction valence electrons, which eventually lead to the switching between p- and n-type conduction, i.e., in Bi_{Pb}, Bi donates three electrons to the Pb vacancy via the following eqn (6):

$$Bi + V_{Pb}^{''} \rightarrow Bi_{Pb} + 1e^- \quad (6)$$

and thus, excess electrons remain in the system, leading to n-type conduction. This difference in conduction type with the increase in temperature for $x = 0.8$ and 0.9 is evident in the plot

of Seebeck coefficient *vs. T*. Thus, the defect thermodynamics as explained above demonstrates as well as dictates the conduction type of the thermoelectric alloy. The prevalence of donor-like antisite defects, Bi_{Ag}, influences the p-type conduction, whereas the presence of supersaturated anionic site with uncompensated cationic antisite defects forestalls n-type conduction at ambient temperature. Nevertheless, the loss of anions with high vapour pressure is inevitable in few instances and thus changes the conduction type accordingly.[50] This analysis displays the effect of phase boundary mapping to control the conduction type of the alloy. In a study by Pan *et al.*, Pb was doped at the Bi site in $AgBiSe_2$, and Pb acts as a hole donor.[33] Thus, a small concentration of Pb retains the n-type conduction of $AgBi_{1-x}Pb_xSe_2$. However, when the concentration of Pb^{2+} exceeds the intrinsic carrier concentration, *i.e.*, electrons, the alloy transforms into p-type. This tuneable engineering in the conduction type can be used for the fabrication of devices.

To further explain the unusual trend in the case of $x \geq 0.8$, we simulated these materials. As the electronic structure of a material is known to have huge influence on the transport properties, we determined the electronic structure of pristine and alloyed PbSe. Although DFT is known to underestimate the band gap due to the approximations, it can provide a qualitative insight.[53] Cubic PbSe showed a principal band gap of 0.16 eV at Γ point (Fig. 5(a)), which is comparable to the values in a previous report.[54] The folding of L point onto the Γ point leads to the appearance of the principal band gap here, as is seen in previous reports of other thermoelectric materials where the same dimensions of supercell were used.[55,56] A band offset of 0.23 eV is estimated between the valence sub-bands at Γ point and $Z + \delta$

point in $Z \rightarrow R$ direction, along with an offset of 0.46 eV between the conduction sub-bands, respectively. The valence and conduction sub-bands with heavy hole nature appear at $Z + \delta$ point in $Z \rightarrow R$ direction in the supercell used, due to folding of the Σ point of the primitive cell's Brillouin zone onto it.[57,58] To further understand the contributions from various atoms, we studied the pDOS (Fig. 5(b)). Se 'p' orbitals form most of the valence band, while 'p' orbitals of Pb form the conduction band, with the Fermi level lying in the mid-gap area.

The alloying of AgBiSeS in PbSe was simulated in a disordered way to mimic the experimental configuration (Fig. 5(c) and (d)). The electronic structure shows a drastic change, with the appearance of new sets of bands traversing across the band gap, touching the valence band at Γ point and conduction band at Z point. The conduction and valence band edges move 0.87 eV apart, with the hybrid band having a width of 1.25 eV. When we examine the pDOS for its content in this area, we see that the 'p' orbitals of Bi and Se hybridize, resulting in increased density of states in this region. Meanwhile, 'p' orbitals of Se and S show major contribution in the valence band region, and the 'p' orbitals of Pb show a considerable contribution 1 eV above the Fermi level. A previous report suggested that Bi does not exert much influence on the electronic structure or pDOS of PbSe, and the present work shows that in the presence of Ag and S, it greatly distorts the DOS.[59] Hybridizing with the anionic orbitals of the host and distorting the DOS is a well-known feature exhibited by Bi in host systems like GeTe and SnTe.[60,61] Although Ag is known to increase the band gap in the systems mentioned above, in the present scenario, it has little to no influence.[62] We do see a cumulative convergence of the valence sub-bands in the alloyed composition leading to an
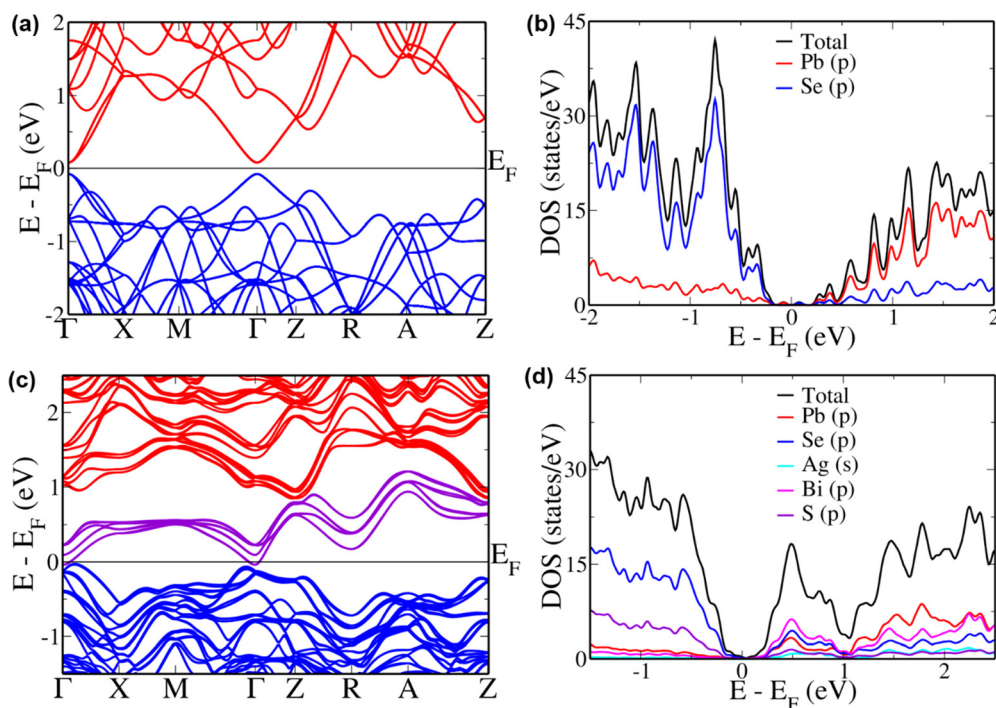

Fig. 5 Electronic structures and pDOS of (a) and (b) PbSe and (c) and (d) AgBiSeS alloyed PbSe. Energies are shifted with respect to Fermi level, which is set to zero.

increase in the number of contributing valleys to the p-type transport. For the improvement of n-type transport, we see the flattening of the conduction bands observed similar to the case of Cd-doped PbSe.[54]

The temperature-dependent electrical resistivity (ρ) of pristine AgBiSeS and those of the $(AgBiSeS)_{1-x}(PbSe)_x$ composites are shown in Fig. 4(b). At ambient temperature (*i.e.* 300 K), the ρ value for AgBiSeS is found to be 112 792 μΩ m, which decreases to 59 μΩ m at 823 K—a reduction in resistivity by 99.9%. This typically indicates semiconductor behaviour, where the degenerate behaviour supersedes the intrinsic excitation and so prevails for all the new alloys formed by using AgBiSeS and PbSe. Moreover, the resistivity plot demonstrates that the resistivities of the entropy-engineered new multinary alloys are lower than that of pristine AgBiSeS. This is attributed to the fact that PbSe, being a degenerate semiconductor, injects electrons in the system and thus optimizes the carrier concentration. However, for $x = 0.5$, there is a competition between the formation of donor type charged antisite defects Bi_{Ag} and Ag_{Pb}. Consequently, in the presence of two donor atoms Bi and Ag, the resistivity drops down in comparison to other alloy systems. Nevertheless, pristine PbSe exhibits the behaviour of a degenerate semiconductor, where the resistivity increases with the increase in temperature (Fig. S4(b), ESI†). The calculated power factor for AgBiSeS and the $(AgBiSeS)_{1-x}(PbSe)_x$ composites are shown in Fig. 4(c).

3.3. Temperature-dependent thermal transport behaviour

Considering the temperature-dependent thermal transport behaviour, the total thermal conductivities (κ) of the pristine AgBiSeS and the solid solutions $(AgBiSeS)_{1-x}(PbSe)_x$, respectively are shown in Fig. 6(a). (Temperature-dependent thermal diffusivity plots of pristine AgBiSeS, PbSe and solid solution of $(AgBiSeS)_{1-x}(PbSe)_x$ are shown in Fig. S5, ESI†). Pan *et al.* reported that $AgBiSe_2$ has a κ value of 0.65 W m^{-1} K^{-1},[33] whereas Hu *et al.* reported a similar composition exhibited the κ of 0.55 W m^{-1} K^{-1}.[40] The total thermal conductivities of the alloys remain significantly flat, demonstrating glass-like behaviour. In the present study, pristine AgBiSeS displays an ultra-low total thermal conductivity of 0.69–0.74 W m^{-1} K^{-1} in the temperature regime of 300–823 K, whereas PbSe exhibits values ranging from 3.16–1.89 W m^{-1} K^{-1} (Fig. S4(d), ESI†). It is noteworthy that AgBiSeS as well as the composites exhibit ultra-low total thermal conductivity over the entire temperature range. Primarily, the total thermal conductivity is constituted by the contributions from the lattice and electronic thermal conductivity. In principle, the lattice thermal conductivity (κ_{lat}) is estimated by directly subtracting the electronic contribution (κ_{ele}) from the total thermal conductivity as $\kappa_{total} = \kappa_{lat} + \kappa_{ele}$. The electronic contribution κ_{ele}, can be estimated using the Widemann Franz Law, $\kappa_{ele} = L\sigma T$, where L is the Lorentz number, σ is the electrical conductivity and T is the temperature. The common practice in thermoelectrics is to consider $L = 2.44 \times 10^{-8}$ W Ω K^{-2} (degenerate limit). Moreover, the Widemann Franz Law is valid for degenerate semiconductors and metals. Thus, utmost care should be taken while estimating κ_{ele}, and so, L was obtained based on the thermopower measured. Kim *et al.* explicitly mentioned that remarkable divergence from the degenerate limit ($\sim$40% or greater for Kane
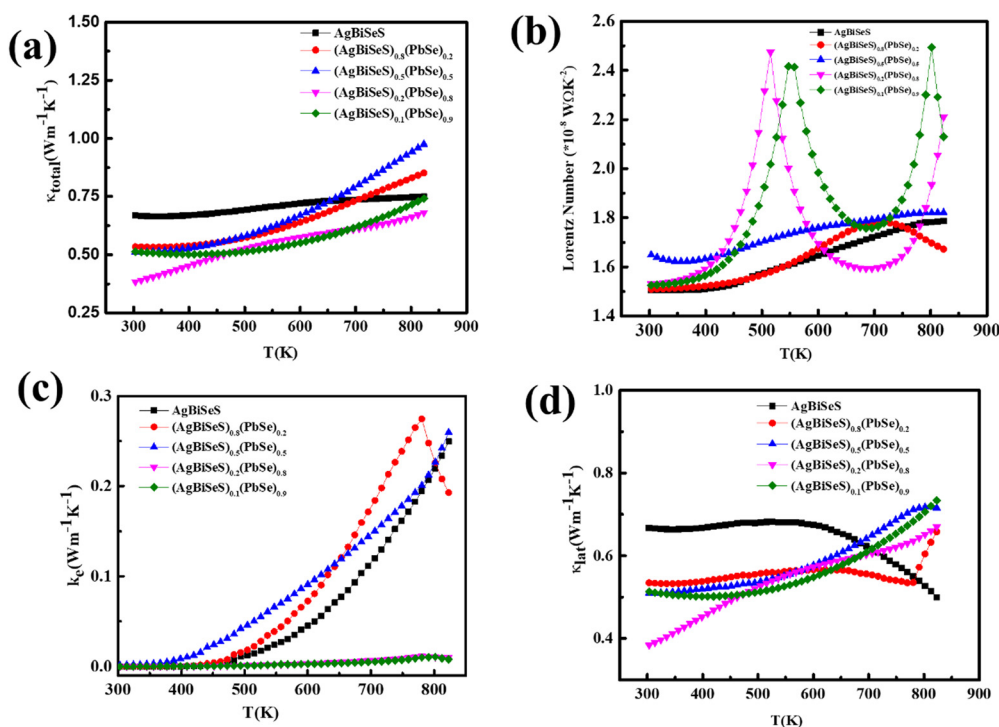

Fig. 6 Temperature-dependent (a) total thermal conductivity; (b) Lorentz number calculated using the Seebeck coeff. values; (c) electronic thermal conductivity; and (c) lattice thermal conductivity of the alloy system $(AgBiSeS)_{1-x}(PbSe)_x$.

bands) are known to arise for non-degenerate semiconductors, and eventually L congregates to 1.5×10^{-8} W Ω K^{-2} (in the case of acoustic phonon scattering). In this regard, L was estimated using the equation $L = 1.5 + \exp\left[\dfrac{-|\alpha|}{116}\right]$.[63] The L estimated using this eqn. for AgBiSeS and $(AgBiSeS)_{1-x}(PbSe)_x$ (x = 0.2, 0.5, 0.8, 0.1) alloy systems was found to be ∼1.5 × 10^{-8} W Ω K^{-2}. However, for the degenerate semiconductor PbSe, L was estimated to be ∼2.44 × 10^{-8} W Ω K^{-2} (Fig. S3(e), ESI†). The L $vs.$ T plot for the compositions under study and the calculated κ_{ele} $vs.$ T are shown in Fig. 6(b) and (c), respectively.

Nevertheless, it is the lattice thermal conductivity which plays the key role in the total thermal conductivity of the alloy without PbSe. When calculated, it shows that without PbSe, where the electronic contribution to κ_{total} is ∼52%, (Fig. S4(d), ESI†), AgBiSeS imparts only 0.006% at RT. On increasing the concentration of PbSe (x = 0.2) in the alloy, the electronic contribution increases marginally; however, at x = 0.5, the electronic contribution to κ_{total} is ∼0.3%. For the compositions x = 0.8 and 0.9, electronic thermal conductivity is almost temperature independent throughout the temperature range. Fig. 6(d) displays the lattice thermal conductivity as a function of T. Previous reports pertaining to I–V–VI$_2$ compounds demonstrate that highly symmetrical rock-salt cubic structures exhibit low κ_{lat} in comparison to other crystal structures, which can be correlated to the intense anharmonicity appearing from the existence of the lone pair electron.[64] Nielsen et al. demonstrated using DFT calculations that the rock salt structure of the I–V–VI$_2$ family develops soft phonon modes owing to the intense hybridization and repulsion among the lone-pair electrons of the cations (group V) and the anions (group VI) having valence p orbitals.[65] Consequently, the presence of stereochemically active non-bonded electrons or lone pairs in the sp-hybridized bonding orbitals cause the occurrence of high Grüneisen parameter, which causes amplified anharmonicity and subsequently low intrinsic lattice thermal conductivity.[66] This is analogous to AgSbTe$_2$, where the valence configuration of Sb ($i.e.$ 5s^{2}5p^3, the 5s orbital being significantly low in energy

compared to the 5p orbital) fails to undergo hybridization and thus prevents the formation of sp^3 bonds among Sb and Te. Thus, the crystal co-ordination swaps from tetrahedral geometry (AgInTe$_2$) to octahedral geometry (AgSbTe$_2$), and the group V cation exhibits +3 oxidation state and develops polar covalent bond with the group VI anion (chalcogens) by sharing the p-electrons. However, the s^2 electrons remain isolated as non-bonding electrons or lone pairs. Eventually, it couples or gets repelled from the valence bands of the d-orbital of noble metals (such as Ag) and the p-orbitals of chalcogen and undergoes deformation (s-orbital of group V) by lattice vibrations, causing strong anharmonicity. In a similar group (Vb), Bi exhibits a large atomic radius (=143 pm) in comparison to Sb (=133 pm),[67] and consequently, it can be assumed or is rather reasonable that the electron cloud encasing the Bi atoms would be higher than Sb. This infers that non-bonded or lone-pair electrons on Bi probably cause more disproportionate electron density, leading to enhanced lattice vibrations. Hence, it can be speculated that pristine AgBiSeS, without PbSe, exhibits ultra-low lattice thermal conductivity owing to enhanced bond anharmonicity related to Bi^{3+} ion and is analogous to the aforementioned Sb^{3+} ion.

3.4. Microstructural analysis

Scanning electron micrographs of the $(AgBiSeS)_{0.5}(PbSe)_{0.5}$ are depicted in Fig. 7(a) and (b). The image shows the sample is highly dense. EDS mapping of the randomly selected region corroborates the homogeneous distribution of the constituent elements and is devoid of any precipitation or phase segregation Fig. 7(c)–(i). (The SEM micrographs along with EDS mapping of other compositions are shown in Fig. S6, ESI†). However, further investigation of the microstructure using high-resolution transmission electron microscopy (HRTEM) depicts the presence of defects at various length scales (majority being point defects due to atomic mass mismatch, Fig. 7(j)). Thus, in spite of the subdued effect of the stereochemical activity of the lone pair on Bi owing to the increase of the chemical space due to entropy engineering, the eventual generation of point defects
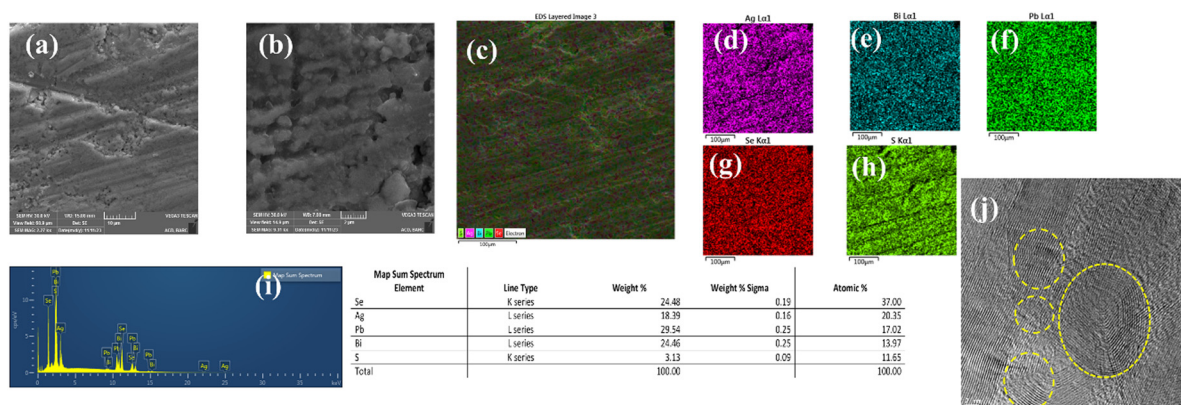

Fig. 7 (a) and (b) SEM micrographs of $(AgBiSeS)_{0.5}(PbSe)_{0.5}$; (c) area pertaining to elemental mapping; (d)–(h) mapping of the constituent elements in the sample depicting the homogeneity; (i) elemental distribution in the sample by EDX; (j) TEM image depicting the presence of hierarchical features at various scales in the sample.
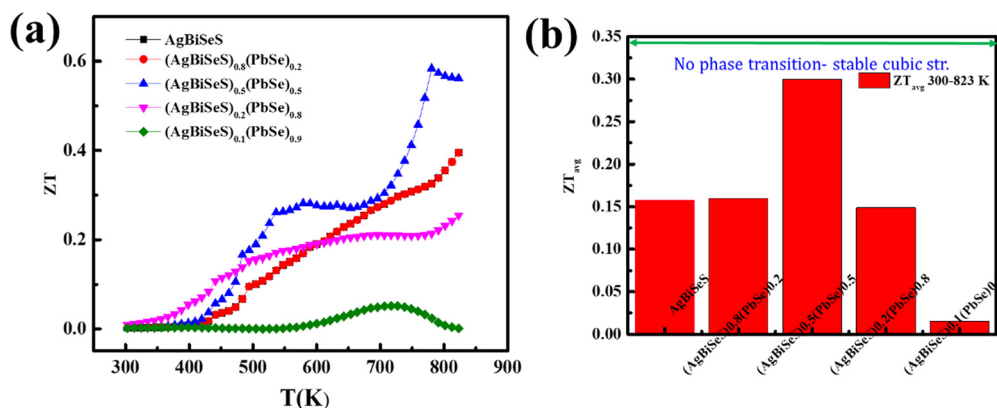
Fig. 8 (a) *ZT vs. T* plot of the alloy system and (b) *ZT*$_{avg}$ *vs.* composition in the temperature range of 300–823 K.

in conjunction with lattice anharmonicity scatters the phonons extensively and thus reduces the lattice thermal conductivity drastically.

Consequently, besides being intrinsically a low-thermal-conductivity alloy, the presence of all-scale hierarchical architecture further slashes the thermal conductivity.

3.5. ZT optimisation

Interestingly, the intrinsic low lattice thermal conductivity attributed to the stereochemical activity of the lone pair on Bi (group Vb) and the large Grüneisen parameter with intentional architecturing in the dimension of the defects, along with entropy-driven structural stabilization, has led to a peak *ZT* of ~ 0.6 at 780 K (Fig. 8(a)) and an average *ZT* value of 0.3 for the alloy $(AgBiSeS)_{0.5}(PbSe)_{0.5}$ within 300–823 K (Fig. 8(b)). To ascertain the repeatability and reproducibility of the $(AgBiSeS)_{0.5}(PbSe)_{0.5}$ composite, samples with nomenclature S1–S6 were measured, and the plot is given in Fig. S7 (ESI†).

4. Conclusion

In conclusion, the stabilized n-type cubic phase of AgBiSeS was synthesized with utmost care, utilizing the concept of phase boundary mapping, as the practical application of thermoelectricity has no space for polymorphism in the operating temperature regime. This excellent dynamical stability was possible owing to the substitution of Se by the highly electronegative S atom, which aids in chemical bond strengthening. This highly susceptible cubic AgBiSeS was further stabilized by entropy-driven solid solution alloying with PbSe. The various analytical techniques corroborate the absence of phase transformation and support the compound as an excellent alternative for an n-type alloy in the mid-temperature (300–823) K regime. Ultra-low lattice thermal conductivity was achieved due to high Grüneisen parameter and bond anharmonicity, in addition to all-scale hierarchical architecturing. Thus, entropy engineering has led to a highly symmetrical cubic structure with diminished thermal conductivity, paving a new path for the design and development of new thermoelectric materials.

5. Author contributions

Ranita Basu: conceptualization, methodology, funding acquisition, investigation, resources, supervision, writing – review and editing; U. Sandhya Shenoy and D. Krishna Bhat: DFT analysis, validation and writing draft, funding acquisition; Ankita Pathak – XPS analysis; Shweta Singh and Hirakendu Basu: morphological and compositional analysis; P. Jha: Raman spectroscopy measurements, and Ajay Singh: Resources.

Data availability

The data supporting this article have been included as part of the ESI.†

Conflicts of interest

There is no conflict of interest.

Acknowledgements

References

1 H. J. Goldsmid and G. S. Nolas, A review of the new thermoelectric materials, Proceedings ICT2001, *20 International Conference on Thermoelectrics (Cat. No. 01TH8589)*, Beijing, China, 2001, pp. 1–6.

2 W. Liu, Q. Jie, H. Seok Kim and Z. Ren, Current progress and future challenges in thermoelectric power generation: from materials to devices, *Acta Mater.*, 2015, **87**, 357–376.

3 D. K. Aswal, R. Basu and A. Singh, Key issues in development of thermoelectric power generators: high figure-of-merit materials and their highly conducting interfaces with metallic interconnects, *Energy Convers. Manage.*, 2016, **114**, 50–67.

4 X.-L. Shi, J. Zou and Z.-G. Chen, Advanced Thermoelectric Design: From Materials and Structures to Devices, *Chem. Rev.*, 2020, **120**, 7399–7515.

5 R. Basu, Thermoelectric Modules: Key Issues in Architectural Design and Contact Optimization, *ChemNanoMat*, 2023, **9**, 1–20.

6 Y. Tian, G.-K. Ren, Z. Wei, Z. Zheng, S. Deng, L. Ma, Y. Li, Z. Zhou, X. Chen, Y. Shi and Y.-H. Lin, Advances of thermoelectric power generation for room temperature: applications, devices, materials and beyond, *Renewable Energy*, 2024, **226**, 120443.

7 J. Li, Q. Xiang, R. Ze, M. Ma, S. Wang, Q. Xie and Y. Xiang, Thermal and electrical analysis of SiGe thermoelectric unicouple filled with thermal insulation materials, *Appl. Therm. Eng.*, 2018, **134**, 266–274.

8 R. Basu and A. Singh, High temperature Si–Ge alloy towards thermoelectric applications: a comprehensive review, *Mater. Today Phys.*, 2021, **21**, 100468.

9 C. Xiao, Z. Li, K. Li, P. Huang and Y. Xie, Decoupling Interrelated Parameters for Designing High Performance Thermoelectric Materials, *Acc. Chem. Res.*, 2014, **47**, 1287–1295.

10 Y. Pei, H. Wang and G. J. Snyder, Band Engineering of Thermoelectric Materials, *Adv. Mater.*, 2012, **24**, 6125–6135.

11 W. Kim, Strategies for engineering phonon transport in thermoelectrics, *J. Mater. Chem. C*, 2015, **3**, 10336–10348.

12 A. Seif, W. DeGottardi, K. Esfarjani and M. Hafezi, Thermal management and non-reciprocal control of phonon flow via optomechanics, *Nat. Commun.*, 2018, **9**, 1207.

13 Q. Tang, B. Jiang, K. Wang, W. Wang, B. Jia, T. Ding, Z. Huang, Y. Lin and J. He, High-entropy thermoelectric materials, *Joule*, 2024, **8**, 1641–1666.

14 B. Jiang, Y. Yu, H. Chen, J. Cui, X. Liu, L. Xie and J. He, Entropy engineering promotes thermoelectric performance in p-type chalcogenides, *Nat. Commun.*, 2021, **12**, 3234.

15 R. Basu and A. Singh, A comprehensive review of entropy engineered GeTe: an antidote to phase transformation, *Energy Adv.*, 2024, **3**, 689–711.

16 P.-C. Wei, C.-N. Liao, H.-J. Wu, D. Yang, J. He, G. V. Biesold-McGee, S. Liang, W.-T. Yen, X. Tang, J.-W. Yeh, Z. Lin and J.-H. He, Thermodynamic Routes to Ultralow Thermal Conductivity and High Thermoelectric Performance, *Adv. Mater.*, 2020, **32**, 1906457.

17 R. K. Pittkowski, C. M. Clausen, Q. Chen, D. Stoian, W. van Beek, J. Bucher, R. L. Welten, N. Schlegel, J. K. Mathiesen, T. M. Nielsen, J. Du, A. W. Rosenkranz, E. D. Bojesen, J. Rossmeisl, K. M. O. Jensen and M. Arenz, The more the better: on the formation of single-phase high entropy alloy nanoparticles as catalysts for the oxygen reduction reaction, *EES Catal.*, 2023, **1**, 950–960.

18 A. D. LaLonde, Y. Pei, H. Wang and G. Jeffrey Snyder, Lead telluride alloy thermoelectrics, *Mater. Today*, 2011, **14**, 526–532.

19 P. Kumar Sharma, T. D. Senguttuvan, V. Kumar Sharma and S. Chaudhary, Revisiting the thermoelectric properties of lead telluride, *Mater. Today Energy*, 2021, **21**, 100713.

20 Y. Pei, N. A. Heinz, A. LaLonde and G. Jeffrey Snyder, Combination of large nanostructures and complex band structure for high performance thermoelectric lead telluride, *Energy Environ. Sci.*, 2011, **4**, 3640–3645.

21 R. Moshwan, L. Yang, J. Zou and Z.-G. Chen, Eco-Friendly SnTe Thermoelectric Materials: Progress and Future Challenges, *Adv. Funct. Mater.*, 2017, **27**, 1703278.

22 Y. Zhang, J. Sun, J. Shuai, X. Tang and G. Tan, Lead-free SnTe-based compounds as advanced thermoelectrics, *Mater. Today Phys.*, 2021, **19**, 100405.

23 S. Ahmad, A. Singh, S. Bhattacharya, M. Navaneethan, R. Basu, R. Bhatt, P. Sarkar, K. N. Meshram, K. P. Muthe, S. Vitta and D. K. Aswal, Remarkable improvement of thermoelectric figure-of-merit in SnTe through in situ-created Te nanoinclusions, *ACS Appl. Energy Mater.*, 2020, **3**, 7113–7120.

24 S. Mandava, R. Basu, B. Khasimsaheb, S. Bathula, A. Singh and S. Neeleshwar, A synergistic approach to achieving the high thermoelectric performance of La-doped SnTe using resonance state and partial band convergence, *Mater. Adv.*, 2021, **2**, 4352–4361.

25 G. Tan, S. Hao, S. Cai, T. P. Bailey, Z. Luo, I. Hadar, C. Uher, V. P. Dravid, C. Wolverton and M. G. Kanatzidis, All-Scale Hierarchically Structured p-Type PbSe Alloys with High Thermoelectric Performance Enabled by Improved Band Degeneracy, *J. Am. Chem. Soc.*, 2019, **141**, 4480–4486.

26 Y. Lee, S.-H. Lo, C. Chen, H. Sun, D.-Y. Chung, T. C. Chasapis, C. Uher, V. P. Dravid and M. G. Kanatzidis, Contrasting role of antimony and bismuth dopants on the thermoelectric performance of lead selenide, *Nat. Commun.*, 2014, **5**, 3640.

27 Y. Wu, P. Qiu, Y. Yu, Y. Xiong, T. Deng, O. Cojocaru-Mirédin, M. Wuttig, X. Shi and L. Chen, High-performance and stable AgSbTe$_2$-based thermoelectric materials for near room temperature applications, *J. Materiomics*, 2022, **8**, 1095–1103.

28 T. Ghosh, S. Roychowdhury, M. Dutta and K. Biswas, High-Performance Thermoelectric Energy Conversion: A Tale of Atomic Ordering in AgSbTe$_2$, *ACS Energy Lett.*, 2021, **6**, 2825–2837.

29 S. Roychowdhury, T. Ghosh, R. Arora, M. Samanta, L. Xie, N. Kumar Singh, A. Soni, J. He, U. V. Waghmare and K. Biswas, Enhanced atomic ordering leads to high thermoelectric performance in AgSbTe$_2$, *Science*, 2021, **371**, 722–727.

30 Y. Zhang, Z. Li, S. Singh, A. Nozariasbmarz, W. Li, A. Genç, Y. Xia, L. Zheng, S. H. Lee, S. K. Karan, G. K. Goyal, N. Liu, S. M. Mohan, Z. Mao, A. Cabot, C. Wolverton, B. Poudel and S. Priya, Defect-Engineering-Stabilized AgSbTe$_2$ with High Thermoelectric Performance, *Adv. Mater.*, 2023, **35**, 2208994.

31 R. Freer and A. V. Powell, Realising the potential of thermoelectric technology: a Roadmap, *J. Mater. Chem. C*, 2020, **8**, 441–463.

32 S. N. Guin, V. Srihari and K. Biswas, Promising thermoelectric performance in n-type AgBiSe$_2$: effect of aliovalent anion doping, *J. Mater. Chem. A*, 2015, **3**, 648–655.

33 L. Pan, D. Berardan and N. Dragoe, High Thermoelectric Properties of n-Type AgBiSe$_2$, *J. Am. Chem. Soc.*, 2013, **135**, 4914.

34 T. Deng, J. Recatala-Gomez, M. Ohnishi, D. V. Maheswar Repaka, P. Kumar, A. Suwardi, A. Abutaha, I. Nandhakumar, K. Biswas, M. B. Sullivan, G. Wu, J. Shiomi, S.-W. Yang and

K. Hippalgaonkar, Electronic transport descriptors for the rapid screening of thermoelectric materials, *Mater. Horiz.*, 2021, **8**, 2463–2474.

35 T. Zhao, H. Zhu, B. Zhang, S. Zheng, N. Li, G. Wang, G. Wang, X. Lu and X. Zhou, High thermoelectric performance of tellurium-free n-type $AgBi_{1-x}Sb_xSe_2$ with stable cubic structure enabled by entropy engineering, *Acta Mater.*, 2021, **220**, 117291.

36 N. Li, G. Wang, Z. Zhou, G. Wang, G. Han, X. Lu and X. Zhou, IV-VI/I–V–VI2 Thermoelectrics: Recent Progress and Perspectives, *Adv. Funct. Mater.*, 2024, 2405158.

37 X. Wu, Y. Lin, C. Liu, Y. Wang, H. Li, B. Ge and W. Liu, A high performance eco-friendly MgAgSb-based thermoelectric power generation device near phase transition temperatures, *Energy Environ. Sci.*, 2024, **17**, 2879–2887.

38 Y.-L. Pei, H. Wu, J. Sui, J. Li, D. Berardan, C. Barreteau, L. Pan, N. Dragoe, W.-S. Liu, J. He and L.-D. Zhao, High thermoelectric performance in n-type BiAgSeS due to intrinsically low thermal conductivity, *Energy Environ. Sci.*, 2013, **6**, 1750–1755.

39 Q. Xia, P. Ying, Z. Han, X. Li, L. Xu and J. Cui, Chemical Composition Engineering Leading to the Significant Improvement in the Thermoelectric Performance of $AgBiSe_2$-Based n-Type Solid Solutions, *ACS Appl. Energy Mater.*, 2021, **4**, 2899–2907.

40 Y. Hu, S. Yuan, H. Huo, J. Xing, K. Guo, X. Yang, J. Luo, G.-H. Rao and J.-T. Zhao, Stabilized cubic phase $BiAgSe_{2-x}S_x$ with excellent thermoelectric properties via phase boundary engineering, *J. Mater. Chem. C*, 2021, **9**, 6766.

41 H. Zhu, T. Zhao, B. Zhang, Z. An, S. Mao, G. Wang, X. Han, X. Lu, J. Zhang and X. Zho, Entropy Engineered Cubic n-Type $AgBiSe_2$ Alloy with High Thermoelectric Performance in Fully Extended Operating Temperature Range, *Adv. Energy Mater.*, 2020, **11**, 2003304.

42 C. A. Gearhart, Einstein before 1905: the early papers on statistical mechanics, *Am. J. Phys.*, 1990, **58**, 468–480.

43 C. Xiao, X. Qin, J. Zhang, R. An, J. Xu, K. Li, B. Cao, J. Yang, B. Ye and Y. Xie, High thermoelectric and reversible p–n–p conduction type switching integrated in dimetal chalcogenide, *J. Am. Chem. Soc.*, 2012, **134**, 18460–18465.

44 Y. Yin, R. M. Rioux, C. K. Erdonmez, S. Hughes, G. A. Somorjai and A. Paul Alivisatos, Formation of Hollow Nanocrystals Through the Nanoscale Kirkendall Effect, *Science*, 2004, **304**, 711–714.

45 W.-T. Chang, S. Sharma, J.-H. Liao, S. Kahlal, Y.-C. Liu, M.-H. Chiang, J.-Y. Saillard and C. W. Liu, Heteroatom-Doping Increases Cluster Nuclearity: From an $[Ag_{20}]$ to an $[Au_3Ag_{18}]$ Core, *Chem. – Eur. J.*, 2018, **24**, 14352.

46 A. Arulraj, N. Ilayaraja, V. Rajeshkumar and M. Ramesh, Direct Synthesis of cubic shaped Ag_2S on Ni mesh as Binder-free Electrodes for Energy Storage Applications, *Sci. Rep.*, 2019, **9**, 10108.

47 S. Gautam, V. Aggarwal, B. Singh, V. P. S. Awana, R. Ganesan and S. S. Kushvaha, Signature of weak-antilocalization in sputtered topological insulator Bi_2Se_3 thin films with varying thickness, *Sci. Rep.*, 2022, **12**, 9770.

48 B. Weng, X. Zhang, N. Zhang, Z.-R. Tang and Y.-J. Xu, Two-Dimensional MoS_2 Nanosheet-Coated Bi_2S_3 Discoids: Synthesis, Formation Mechanism, and Photocatalytic Application, *Langmuir*, 2015, **31**, 4314–4322.

49 W. Huang, Y. Zhu, Y. Liu, S. Tao, C. Yang, Q. Diao, Z. Hong, H. Han, L. Liue and W. Xu, Long-range ordering and local structural disordering of $BiAgSe_2$ and BiAgSeTe thermoelectrics, *Phys. Chem. Chem. Phys.*, 2021, **23**, 24328.

50 H. Jang, M. Y. Toriyama, S. Abbey, B. Frimpong, J. P. Male, G. Jeffrey Snyder, Y. Sik Jung and M.-W. Oh, Suppressing Charged Cation Antisites via Se Vapor Annealing Enables p-Type Dopability in $AgBiSe_2$–SnSe Thermoelectrics, *Adv. Mater.*, 2022, **34**, 2204132.

51 R. Shannon, Revised effective ionic radii and systematic studies of interatomic distances in halides and chalcogenides, *Acta Crystallogr.*, 1976, **32**, 751.

52 Q. Tian, P. Li, L. Zhang, Y. Tian, L.-J. Yin, L. Zhang and Z. Qin, Native Pb vacancy defects induced p-type characteristic in epitaxial monolayer PbSe, *Appl. Phys. Lett.*, 2023, **123**, 051903.

53 U. S. Shenoy and D. K. Bhat, Electronic Structure Modulation of $Pb_{0.6}Sn_{0.4}Te$ via Zinc Doping and Its Effect on the Thermoelectric Properties, *J. Alloys Compd.*, 2021, **872**, 159681.

54 X. Qian, H. Wu, D. Wang, Y. Zhang, J. Wang, G. Wang, L. Zheng, S. J. Pennycook and L. D. Zhao, Synergistically optimizing interdependent thermoelectric parameters of n-type PbSe through alloying CdSe, *Energy Environ. Sci.*, 2019, **12**, 1969–1978.

55 D. K. Bhat and U. S. Shenoy, Mg/Ca Doping Ameliorates the Thermoelectrics Properties of GeTe: Influence of Electronic Structure Engineering, *J. Alloys Compd.*, 2020, **834**, 155989.

56 U. S. Shenoy and D. K. Bhat, Vanadium: A Protean Dopant in SnTe for Augmenting its Thermoelectric Performance, *ACS Sustainable Chem. Eng.*, 2021, **9**, 13033–13038.

57 U. S. Shenoy and D. K. Bhat, Towards achieving an ideal convergence of light and heavy electron conduction bands in SnTe: insights into copper doping, *J. Alloys Compd.*, 2024, **1**, 100001.

58 U. S. Shenoy and D. K. Bhat, Tuning the Electronic Structure of Rhombohedral and Cubic GeTe for Thermoelectric Application: Influence of Molybdenum Doping, *J. Phys. Chem. Solids*, 2024, **188**, 111943.

59 M. Hong, W. Lyu, Y. Wang, J. Zou and Z. G. Chen, Establishing the Golden Range of Seebeck Coefficient for Maximizing Thermoelectric Performance, *J. Am. Chem. Soc.*, 2020, **142**, 2672–2681.

60 U. S. Shenoy and D. K. Bhat, Probing of Bi doped GeTe thermoelectrics leads to revelation of resonant states, *J. Alloys Compd.*, 2022, **921**, 165965.

61 U. S. Shenoy and D. K. Bhat, Improving ZT of SnTe by Electronic Structure Engineering: Unusual Behaviour of Bi Dopant in the presence of Pb as a Co-dopant, *Mater. Adv.*, 2021, **2**, 6267–6271.

62 U. S. Shenoy and D. K. Bhat, Selective Co-doping Improves the Thermoelectric Performance of SnTe: An Outcome of Electronic Structure Engineering, *J. Alloys Compd.*, 2021, **892**, 162221.

63 H.-S. Kim, Z. M. Gibbs, Y. Tang, H. Wang and G. Jeffrey Snyder, Characterization of Lorenz number with Seebeck coefficient measurement, *APL Mater.*, 2015, **3**, 041506.

64 M. K. Jana, K. Pal, U. V. Waghmare and K. Biswas, The Origin of Ultralow Thermal Conductivity in InTe: Lone-Pair-Induced Anharmonic Rattling, *Angew. Chem., Int. Ed.*, 2016, **55**, 7792.

65 M. D. Nielsen, V. Ozolins and J. P. Heremans, Lone pair electrons minimize lattice thermal conductivity, *Energy Environ. Sci.*, 2013, **6**, 570–578.

66 R. Basu, C. Nayak, R. Kumar, D. Bhattacharyya, S. N. Jha and A. Singh, Potency of Extended X-ray Absorption Fine Structure Spectroscopy toward the Determination of Individual Bond Grüneisen Parameter for High Thermoelectric Performance, *ACS Appl. Energy Mater.*, 2023, **6**, 2981–2988.

67 **https://periodictable.com/Properties/A/AtomicRadius.v. html**.